 doi:10.20944/preprints202203.0347.v1

Article

Obtaining and characterization of high-quality recycled graphites from different types of spent batteries

Lorena Alcaraz [1,*], Carlos Díaz-Guerra [2] and Félix A. López [1]

[1] Centro Nacional de Investigaciones Metalúrgicas (CENIM), Consejo Superior de Investigaciones Científicas (CSIC), Av. Gregorio del Amo 8, 28040 Madrid, Spain; alcaraz@cenim.csic.es; f.lopez@csic.es
[2] Departamento de Física de Materiales, Facultad de Ciencias Físicas, Universidad Complutense de Madrid, Plaza de Ciencias 1, 28040 Madrid, Spain; cdiazgue@fis.ucm.es
* Correspondence: alcaraz@cenim.csic.es; Tel.: +34 911992202

Abstract: Spent batteries recycling is an important way to obtain low-cost graphite. Nevertheless, the obtaining of crystalline graphite with a rather low density of defects is required for many applications. In the present work, high-quality graphites have been obtained from different kinds of spent batteries. Black masses from spent alkaline batteries (batteries black masses, BBM), and lithium-ion batteries from smartphones (smartphone black masses, SBM) and electric and/or hybrid vehicles (lithium-ion black masses, LBM) were used as starting materials. A hydrometallurgical process was then used to obtain recycled graphites by acidic leaching. Different leaching conditions were used depending on the type of the initial black mass. The final solids were characterized by a wide set of complementary techniques.

Keywords: Recycled graphite; high-quality graphite; spent batteries; acidic leaching

1. Introduction

Circular economy is a regenerative approach to reduce the waste generated and guarantee the eco-sustainability of post-use products. When a product reaches the end of its life, it is reused to generate high added-value materials, which reduces both the need for primary materials and waste production [1,2]. This explains the growing interest among the scientific community to develop and optimize different methods for the recycling and the reuse of waste, especially hazardous waste which requires an adequate management.

Batteries are currently used in many electronic devices, including electric and hybrid vehicles [3,4]. Due to the exponentially increasing number of spent batteries recently generated, the recycling of batteries components has aroused global attention [5]. Spent batteries contain heavy metals which may seep out, negatively affecting the environment and human health [6,7]. The leaching process has successfully been described as a method to dissolve metals present in the black mass, a common waste generated in the recycling of batteries.

Usually, a preliminary phase is carried out for spent batteries preparation (sorting, discharging, and dismantling). Subsequently, spent batteries are pre-treated to generate the active valuable materials through different processes (thermal, mechanical, physical, chemical, or mechano-chemical). Thus, a metals-enriched fraction (called black mass) is obtained.

Previous investigations showed that it is possible to obtain highly pure materials from black masses. Regarding the recycling of the anode material, some investigations have previously reported the recovery of high-quality graphite using mechanical methods from spent lithium-ion batteries (LIBs) [8,9]. In fact, after the leaching process a large amount of insoluble residues remain, mainly composed of carbon. This carbonaceous residue is an excellent precursor which can be turned into a high added-value material such as graphite, which is used in a great variety of electrochemical applications due to its electrical and thermal conductivity, inertness, and resistance.

Preprints (www.preprints.org) | NOT PEER-REVIEWED | Posted: 25 March 2022 doi:10.20944/preprints202203.0347.v1

In addition, it was reported that the demand for high-quality graphite increases between 10%-12% per year [10,11], and the price of graphite of battery-grade was 5000$–20,000$ per ton, in 2016 [11]. Thus, recycled graphite from spent batteries could be an important source of low-cost graphite in the near future.

Several investigations have previously reported the obtaining of high-quality graphite from spent lithium-ion batteries. However, usually black mass from smartphones was used, and anode material was previously separated from cathode material to achieve a higher purity of the final graphite.

In this work, we report on the obtaining of high-added value material from black masses of different batteries. Black masses from both Zn/C alkaline and lithium-ion batteries were used as starting materials. Recycled graphites were obtained by a leaching process with an acidic solution. Different conditions which affect the quality of the final graphite were also assessed. A deep characterization of all obtained recycled graphites was also carried out.

2. Materials and Methods

2.1. Obtaining of recycled graphites

Different black masses from spent batteries have been investigated for the recovery of graphite. Two different sieved powders of black mass, including cathode materials, anode materials, and other metal impurities from spent alkaline batteries and lithium-ion batteries were used in the present work as starting materials.

According to previous investigations [12], it is possible to recover metals through acidic leaching of a black mass from spent alkaline and Zn-C batteries, leading to insoluble materials mainly composed of carbon. Thus, 300 g of washed black mass from spent alkaline batteries (BBM) were put in contact with an acid mixture formed by 250 mL of Milli-Q water, 500 mL of 6 M hydrochloric acid (HCl), and 250 mL of H_2O_2, and dispersed using mechanical stirring at room temperature for 1 h. Then, the mixture was filtered and the final obtained solid (called C-BBM) was dried at 80 ºC for 24 h. In the case of the black mass from LIBs, spent batteries from both smartphones and vehicles were used. In the latter case and for comparison purposes, two different conditions to obtain high-quality material were assessed. The spent smartphone batteries were manually dismantled by the separation of the cathode, anode, and aluminum and plastic cases. The final powder, which corresponds to the anodic fraction, was investigated and labelled C-SBM. Finally, 100 g black mass from vehicles were subjected to acidic leaching using i) 950 mL of 2 M sulphuric acid (H_2SO_4) and 50 mL of H_2O_2, and ii) 990 mL of 1.25 M citric acid ($C_6H_8O_7$) and 10 mL of H_2O_2 at 70 ºC for 2 h. As previously described, the mixtures were filtered and the final solids (called C-L_1BM and C-L_2BM, respectively) were dried at 80 ºC for 24 h. In this sense, previous studies have reported that higher metal contents can be recovered using acidic conditions, which would lead to a more pure graphite [13–15].

The sample notation, starting black mass, and obtaining conditions used in each case are summarized in **Table 1**.

Table 1. Samples notation and obtaining conditions for the investigated samples.

Sample notation	Black mass	Leaching conditions
C-BBM	Black mass from spent Zn/C alkaline batteries	6 M HCl/H_2O_2 (25% v/v)
C-SBM	Black mass from spent smartphone lithium-ion batteries	Untreated
C-L_1BM	Black mass from spent vehicles lithium-ion batteries	2 M H_2SO_4/H_2O_2 (5 % v/v)
C-L_2BM	Black mass from spent vehicles lithium-ion batteries	1.25 M $C_6H_8O_7$/H_2O_2 (1 % v/v)

Preprints (www.preprints.org) | NOT PEER-REVIEWED | Posted: 25 March 2022 doi:10.20944/preprints202203.0347.v1

2.2. Characterization

The chemical composition of the starting black masses was determined by X-ray fluorescence (XRF) analysis using a PANalytical Axios wavelength dispersive spectrometer (4 kW). In addition, carbon content was determined by combustion in an induction furnace combustion and infrared detection system.

The structural characterization of the obtained samples was carried out by X-ray diffraction (XRD) using a Bruker D8 Advance diffractometer with Cu K_α radiation (λ = 1.5406 Å).

The mean interlayer spacing, d_{002}, was determined using the Bragg's equation (**Equation 1**), the graphitization degree (g) was determined using the Franklin equation (**Equation 2**), and the stacking height (L_c) were evaluated using the Scherrer formula (**Equation 3** and **Equation 4**, respectively). These parameters are commonly used to evaluate the degree of structural order of the carbonaceous materials.

$$d_{002}(\text{nm}) = \frac{\lambda}{2\sin\theta} \qquad \text{Eq. 1}$$

$$g(\%) = \frac{0.3340 - d_{002}}{0.3340 - 0.3354} \cdot 100 \qquad \text{Eq. 2}$$

$$L_c(\text{nm}) = \frac{k \cdot \lambda}{\beta_{002} \cdot \cos\theta_{002}} \qquad \text{Eq. 3}$$

In these equations, λ is the X-ray wavelength, θ is the Bragg angle corresponding to the diffraction peak, k is the Scherrer constant (k = 0.94), β is the full width at half maximum (FWHM) of the diffraction peak, 0.3440 is the interlayer spacing of the fully non-graphitized carbon (nm), and 0.3354 is the carbon layer spacings of the ideal graphite crystal (nm), respectively.

The morphology of the samples was investigated with a FEI Inspect S scanning electron microscope (SEM), while its chemical composition and elemental spatial distribution were assessed by energy dispersive X-ray microanalysis (EDX, Bruker Quantax) in a Leica 440 Steroscan SEM. An accelerating voltage of 20 kV and a beam current of 1.5 nA was used for EDX measurements.

Micro-Raman measurements were carried out at room temperature in a Horiba Jovin-Ybon LabRAM HR800 system. The samples were excited by a 633 nm He-Ne laser on an Olympus BX41 confocal microscope with a 100x objective. The spectral resolution of the system used was ~ 1 cm^{-1}. Laser power density was carefully adjusted in order to avoid heating or irradiation effects. Spectra shown in this work were taken under the same experimental conditions for comparison purposes.

3. Results and discussion

3.1. X-ray fluorescence (XRF)

The starting black masses were dried at 80 °C and sieved to obtain representative fractions with particle size below 80 μm. Its chemical composition was determined by X-ray fluorescence (XRF). The obtained results are given in **Table 2**. The group "Others" corresponds to elements found in concentrations below 0.01 wt.% as well as to light elements such as Li, O, and F, including C.

Preprints (www.preprints.org) | NOT PEER-REVIEWED | Posted: 25 March 2022 doi:10.20944/preprints202203.0347.v1

Table 2. Chemical composition (%wt) of the starting black masses. The carbon content appearing in the last row is that determined by combustion in an induction furnace and infrared detection.

Compound	C-BBM	C-SBM	C-LBM
Na_2O	7.75	0.06	-
MgO	0.13	-	-
Al_2O_3	0.46	0.04	2.25
SiO_2	0.19	0.08	0.06
P_2O_5	0.99	0.75	1.08
SO_3	0.64	0.15	0.21
Cl	1.76	-	0.04
K_2O	6.70	-	-
CaO	0.36	-	0.07
TiO_2	0.16	-	0.01
MnO	41.40	0.04	6.45
Fe_2O_3	1.42	0.02	0.03
Co_3O_4	0.03	0.20	4.43
NiO	0.18	-	6.84
CuO	0.08	0.94	1.17
ZnO	26.88	-	0.95
SrO	0.04	-	-
ZrO_2	0.01	-	0.14
CdO	0.01	-	-
SnO_2	0.03	-	0.01
PbO	0.04	-	-
Others	10.74	97.92	76.26
C	5.42	85.59	33.87

In the case of the black mass from spent LIBs, some chemical elements can be associated with a particular component of the battery such as aluminium to the cathode current collector; copper to the anode current collector, and iron to the casing particles. Other metals such as cobalt, nickel, and manganese were also detected and can be associated to the lithium metal oxides.

In addition, carbon content was determined by combustion in an induction furnace and infrared detection, as specified in last row of **Table 2**.

3.2. X-ray diffraction (XRD)

Structural characterization of the final obtained solids was initially carried out by X-ray diffraction. XRD patterns of the investigated samples are shown in **Figure 1**.

Preprints (www.preprints.org) | NOT PEER-REVIEWED | Posted: 25 March 2022 doi:10.20944/preprints202203.0347.v1

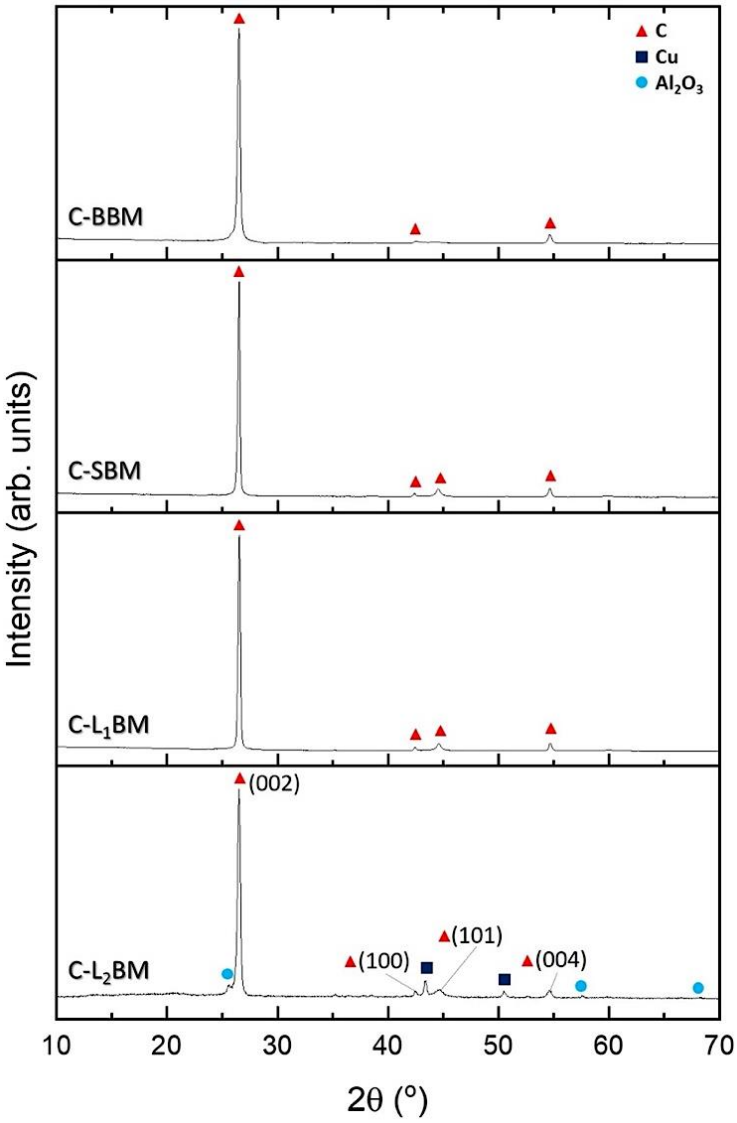

Figure 1. XRD patterns of the obtained final solids.

In all cases, the more intense diffraction maxima were indexed to the carbon-graphite phase with hexagonal structure and space group $P6_3/mmc$ (JCPDS 00-056-0159). The narrower and higher peak centered at around 26.5° can be attributed to the reflection in the (002) plane of aromatic layers. Other peaks centered at 42°, 44°, and 54°, which correspond to the (100), (101), and (004) planes of graphite carbon, can also be observed. The (002) peak is attributed to the orientation of the aromatic ring carbon reticulated layers in three-dimensional arrangement. The (100) peak is related to the degree of condensation of the aromatic ring (i.e. the size of the carbon slice of the aromatic layer [16]). The sharper and the higher the (002) and (100) peaks are, the better the orientation and the larger the size of the aromatic layer slice, respectively.

A comparative analysis of the structural data of the final obtained materials are summarized in **Table 3**. In all cases, the calculated d_{002} of the recycled graphites were very similar that of ideal graphite (0.3354 nm) with d_{002} values < 0.3440 nm. Therefore, they can be classified within graphitic materials. [17]. In addition, graphitization degree was higher than 87 % for all obtained samples. These results suggest that the final obtained samples are high-quality recycled graphites. Finally, the calculated L_c values increase for decreasing d_{002} interlayer spacing.

Preprints (www.preprints.org) | NOT PEER-REVIEWED | Posted: 25 March 2022 doi:10.20944/preprints202203.0347.v1

Table 3. Structural parameters calculated for the graphite samples.

Sample	d_{002} (nm)	g (%)	L_c (nm)
C-BBM	0.3363	87	30.47
C-SBM	0.3358	92	40.62
C-L_1BM	0.3356	96	44.90
C-L_2BM	0.3360	91	32.81

Besides graphite-related diffraction maxima, XRD patterns of the C-L_2BM material also show much weaker peaks that can be attributed to secondary phases, in particular to Al_2O_3 (JCPDS 00-46-1212) and Cu (JCPDS 00-04-0836). As previously mentioned, these impurities can be attributed to cathode and anode current collector, respectively. No more impurities were detected within the sensibility of these measurements.

3.3. Scanning electron microscopy (SEM)

Microstructural characterization of the obtained samples was carried out by scanning electron microscopy (SEM). **Figure 2** shows representative SEM images of the investigated materials. In all cases, agglomerates of densely packed C layers of different sizes were observed. Interspersed among such agglomerates, smaller particles can also be appreciated. However, small differences can be appreciated. C-BBM sample exhibits less packed layers than the other analyzed samples, which size varies between 10 and 200 μm approximately with a flake-like morphology. A similar morphology can be appreciated in the samples obtained from black masses of spent lithium-ion batteries. In these cases, more rounded particle shape was found, with agglomerates sizes in the range of (2-40) μm, (5-20) μm, and (10-30) μm for the C-SBM, C-L_1BM, and C-L_2BM samples, respectively.

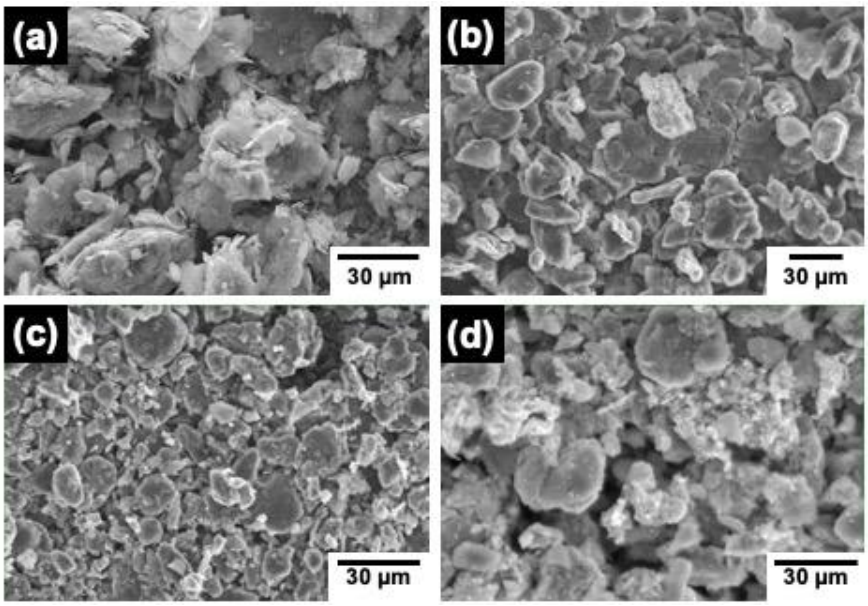

Figure 2. SEM micrographs representative of the investigated samples: (a) C-BBM, (b) C-SBM, (c) C-L_1BM, and (d) C-L_2BM.

3.4. EDX microanalyses

The chemical composition of the samples, as well as their corresponding elemental spatial distribution, were investigated by energy dispersive X-ray microanalysis. In all cases, EDX microanalyses (**Table 4**, and **Figure 3**) reveal that C is the main element in the samples, although the presence of some impurities in low concentrations is clearly detected. Spectra are represented in log scale in order to visualize elements present in lower concentrations more clearly.

Preprints (www.preprints.org) | NOT PEER-REVIEWED | Posted: 25 March 2022 doi:10.20944/preprints202203.0347.v1

In the case of the final materials obtained from black masses of spent lithium-ion batteries, the concentration of fluorine is high. This is due to the presence of the electrolyte in the starting black masses, since electrolyte solutions based on fluorinated solvents are commonly used in LIBs because of their extraordinary electrochemical stability [18,19]. Moreover, copper and silicon were also detected, in good agreement with the obtained results from XRD measurements. Both elements are related to the electrical components and the case of the batteries.

Table 4. Quantification of EDX analyses (normalized %wt) carried out in the final graphite samples.

Element	C-BBM	C-SBM	C-L$_1$BM	C-L$_2$BM
Carbon	80.97	56.4	73.65	55.4
Oxygen	15.07	15.1	14.86	9.523
Barium	1.29	-	-	-
Chlorine	1.20	-	-	-
Iron	0.49	-	-	-
Silicon	0.427	0.1	1.88	0.054
Sulfur	0.279	0.2	-	0.079
Aluminium	0.191	0.1	0.81	3.02
Potassium	0.082	-	-	-
Copper	-	2.4	0.8	3.81
Fluorine	-	54	7.85	28
Cobalt	-	0.59	-	-
Phosphorus	-	1.07	0.045	0.066

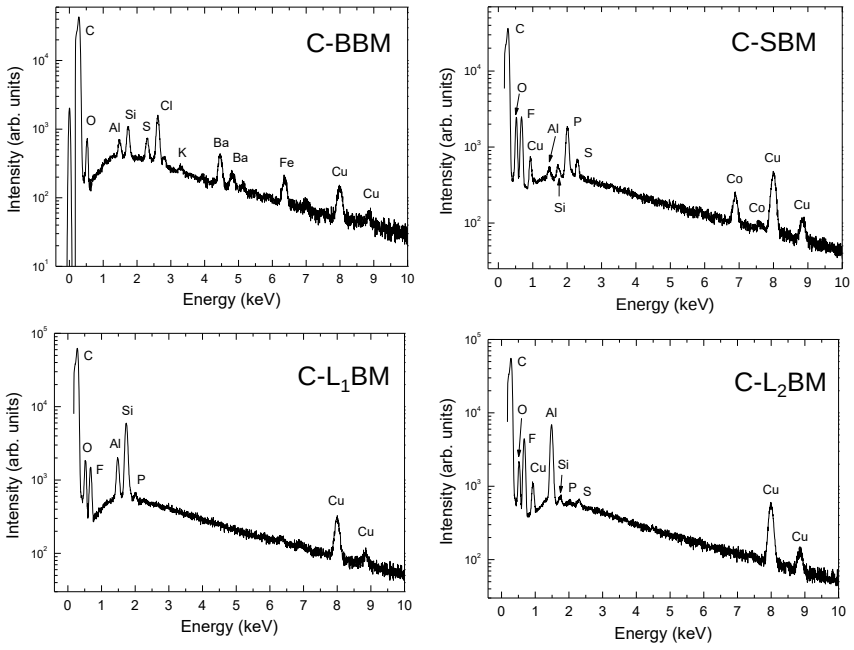

Figure 3. Representative EDX spectra of the investigated graphite samples.

The spatial distribution of the elements detected in the different samples are shown in **Figures 4-7**.

Carbon distribution is homogeneous throughout the whole material in all the investigated samples. No clear correlation seems to exist between the detected elements in the case of the C-BBM sample (**Figure 4**).

The elements detected in the C-SBM sample (**Figure 5**) appear to be quite homogeneously distributed, with the exception of P and Cu. The corresponding mappings reveal that the distributions of these two elements are spatially correlated.

Preprints (www.preprints.org) | NOT PEER-REVIEWED | Posted: 25 March 2022 doi:10.20944/preprints202203.0347.v1

In the case of the C-L1BM material (**Figure 6**), a clear correlation between the distribution of Si and O, as well as between the distribution of Al and O can be appreciated, which strongly suggest the existence of alumina and silica particles in the sample. The absence of diffraction maxima corresponding to silica and alumina can be attributed to the low concentration of these phases and/or their low crystallinity. Although Cu is detected in the EDX spectra, the corresponding mappings revealed no particular feature irrespective of the area sampled or the SEM magnification used, which strongly suggests that the mentioned signal comes from the SEM sample holder.

Finally, the spatial distribution of Al is strongly correlated with that of O in the case of the C-L2BM sample (**Figure 7**), evidencing the existence of alumina particles. Diffraction maxima related to alumina were in fact detected in the XRD pattern of this sample. In addition, the spatial distribution of Cu is not correlated with that of O. Metallic Cu particles with sizes ranging approximately between 1 and 10 μm can be observed in the corresponding mapping, although their surface is probably slightly oxidized due to contact with air. In this sample, Cu signal clearly does not stem from the SEM holder. This result is also in good agreement with our XRD measurements, where Cu diffraction maxima were found.

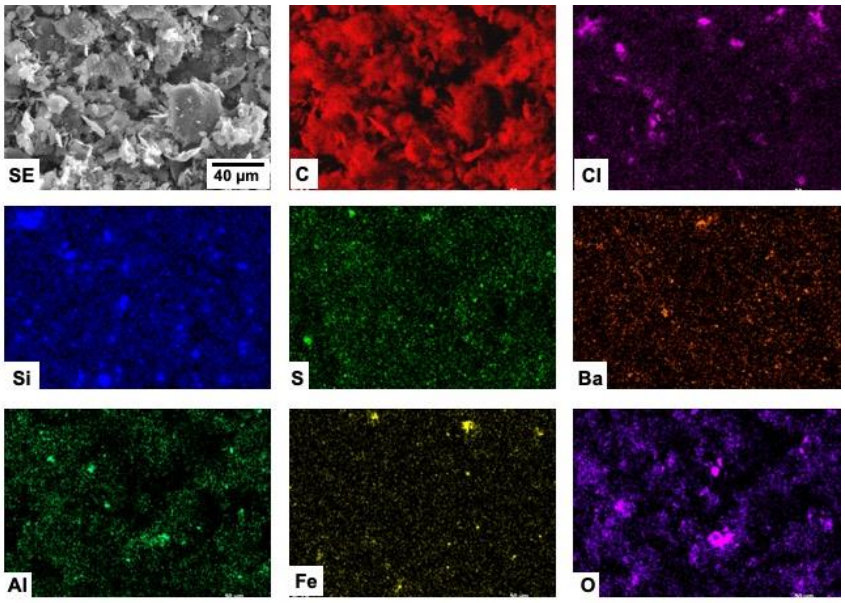

Figure 4. SEM-EDX mappings from sample C-BBM.

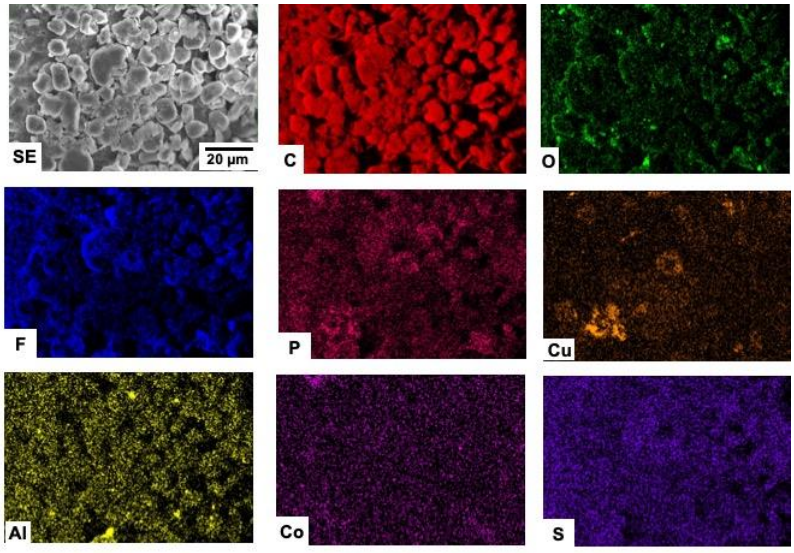

Figure 5. SEM-EDX mappings from sample C-SBM.

Preprints (www.preprints.org) | NOT PEER-REVIEWED | Posted: 25 March 2022 doi:10.20944/preprints202203.0347.v1

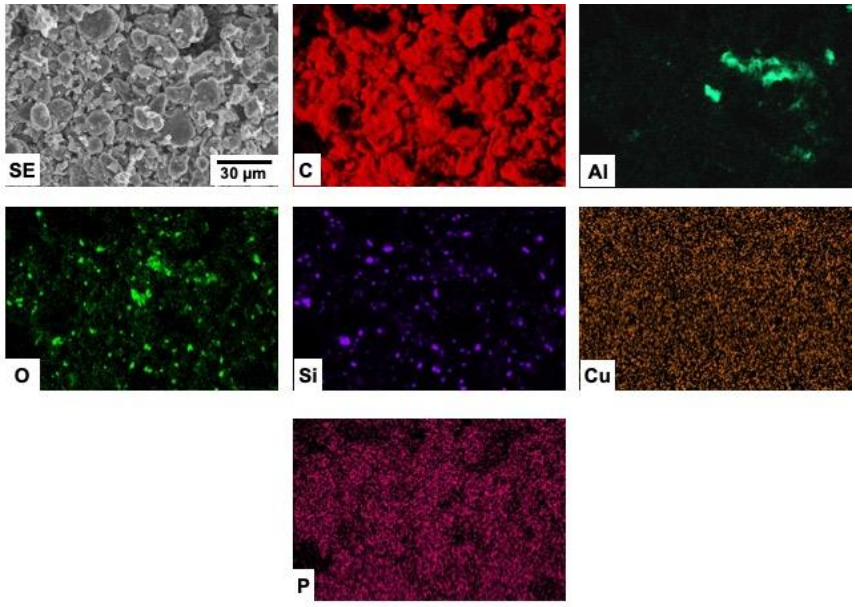

Figure 6. SEM-EDX mappings from sample C-L1BM.

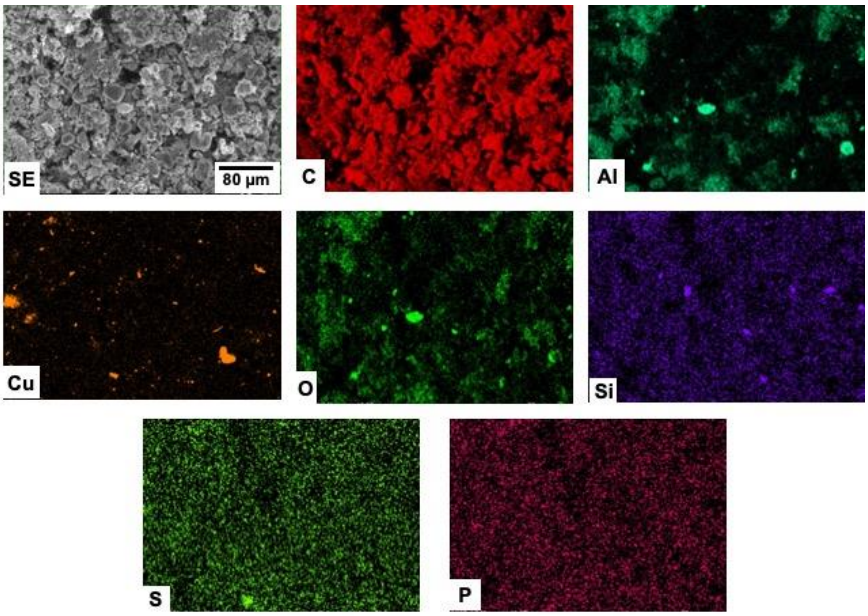

Figure 7. SEM-EDX mappings from sample C-L2BM.

3.5. Micro-Raman spectroscopy

All the obtained samples were also characterized by micro-Raman spectroscopy. This non-destructive spectroscopic technique is particularly suitable for the characterization of C-based compounds, providing information regarding its morphology, defect structure, and graphitization degree, and is an important tool for the characterization of the different carbon allotropes due to its sensitivity to structural changes [20,21]. Representative spectra of each sample are shown in **Figure 8.** Several bands related to different vibrations of C atoms in graphite can be observed. The relative intensities of the mentioned bands were found to depend, to a certain extent, on the size of the particle probed by the laser beam. Their peak positions and corresponding assignments are shown in **Table 5**.

Preprints (www.preprints.org) | NOT PEER-REVIEWED | Posted: 25 March 2022 doi:10.20944/preprints202203.0347.v1

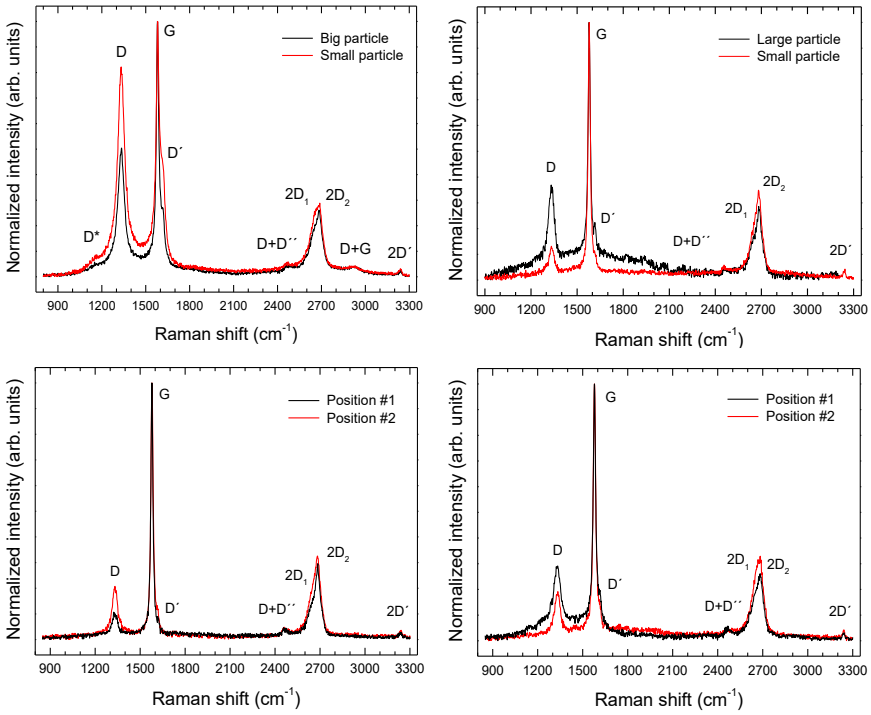

Figure 8. Representative Raman spectra from the (a) C-BBM, (b) C-SBM, (c) C-L1BM, and (d) C-L2BM samples.

Table 5. Raman bands positions (cm^{-1}) observed in the investigated samples and their assignments.

Element	C-BBM	C-SBM	C-L1BM	C-L2BM
D*	~1155	n.o.	n.o.	n.o.
D	1332	1332	1332	1333
G	1581	1579	1579	1578
D´	1615	1617	1619	1616
D+D´´	~2470	~2456	~2458	~2467
$2D_1$	2647	2646	2646	2653
$2D_2$	2686	2686	2686	2685
D+G	2922	n.o. [1]	n.o. [1]	n.o. [1]
2D´	3241	3242	3240	3241

[1] Not observed.

Some of these bands are not evident but found by deconvolution of the experimental data to a sum of Lorentzian profiles. The D peak is a defect-activated band associated to the breathing modes of six-atom rings K-point phonons (A_{1g} symmetry). The D´ band is also related to defects, since it originates from intravalley one-phonon double resonance Raman processes involving one longitudinal optical phonon near the Γ point of the Brillouin zone (BZ) and one defect. These modes are not Raman active in first order Raman scattering of perfect crystals, since they are not zone-center modes, but become Raman active in defective graphitic materials owing to defect-induced double resonance Raman scattering processes involving the electronic π–π* transitions [22]. The G band is a doubly degenerate phonon mode (E_{2g} symmetry) at the BZ center that is due to the bond stretching vibrations of all pairs of sp^2 atoms in both rings and chains of carbon networks [23,24]. The 2D band corresponds to the harmonic (second order Raman scattering) of an in-plane transverse optical (TO) mode close to the zone boundary K point [22]. This band appears as a doublet due to the splitting's of the π and π* electronic states, owing to the interactions between the successive layer planes.

Some bands related to the second order Raman spectrum were also detected. In the case of the C-BBM sample, three weak bands at 2470, 2922, and 3241 cm^{-1}, assigned to the

Preprints (www.preprints.org) | NOT PEER-REVIEWED | Posted: 25 March 2022 doi:10.20944/preprints202203.0347.v1

combinations D+D'', D+G and to the harmonic 2D', respectively, were found. In the other cases only two weak bands at 2456, 2458 and 2467 cm^{-1}, assigned to the combination D+D'', and 3242, 3240, and 3241 cm^{-1} assigned to the harmonic 2D', were detected for the C-SBM, C-L_1BM, and C-L_2BM, respectively. D'' corresponds to a phonon belonging to the in-plane longitudinal acoustic (LA) branch close to the K point [25] and D' corresponds to a phonon of the in-plane longitudinal optical (LO) branch close to the zone center (Γ point) [26]. Besides, in the case of the C-BBM sample, a low-intensity band can be appreciated at about 1155 cm^{-1} (D^* band). The origin of this band is still controversial, since it has been observed in graphene oxide samples with different chemical compositions [27], nanocrystalline diamond [21] and few-layer wrinkled graphene [22], amongst other carbon materials. Some authors attributed the D^* peak to sp^3 carbons in amorphous or disordered graphitic lattices [20,22], while others assign this peak to C=C stretching and CH wagging modes of trans-polyacetylene and not to sp^3 carbons [21], which is unlikely in the present case.

The intensity ratio of the (I_D/I_G) bands reflects the order degree of the graphite [16], the intensity of the D' peak is proportional to the amount of defects [30], while the Full Width at Half Maximum (FWHM) of the G band is known to reflect the surface crystallinity of the carbon material and decreases for increasing crystallite size [31]. The ranges of variation of the intensity ratios I_D/I_G and $I_{D'}/I_G$ as well as the FWHM of the G band measured for each sample are summarized in **Table 6**. According to the obtained results, the relative intensities of the C-BBM sample can be considered representative of a crystalline graphite with a rather high density of defects, as evidenced by the higher (I_D / I_G) and ($I_{D'}$ / I_G) ratios, as well as the higher FWMH of the G band, as compared with that measured in the other samples. Furthermore, the relative intensities of the mentioned bands for the C-SBM, C-L_1BM and C-L_2BM samples can be considered representative of good quality crystalline graphites, with a rather low density of defects. These results are in good agreement with the obtained from XRD measurements, where the C-BBM sample exhibit lower graphitization degree (g, %) than the other analyzed samples.

Table 6. Variation ranges of the intensity ratios I_D/I_G and $I_{D'}/I_G$ and FWHM of the G band for all the samples investigated.

Relative intensity / Sample	C-BBM	C-SBM	C-L_1BM	C-L_2BM
(I_D/I_G)	0.50 – 0.82	0.1 – 0.3	0.11 – 0.21	0.19 – 0.29
($I_{D'}/I_G$)	0.27 – 0.48	0.03 – 0.09	0.03 – 0.05	0.04 – 0.08
FWMH (cm^{-1})	19.6 – 24.9	16.7 – 17.4	16.5 – 17.7	19 – 20

On the other hand, micro-Raman measurements were also carried out in small particles, (1-4) μm in size, of the C-L_2BM sample, showing a different appearance in SEM micrographs.

Some examples are shown in (**Figure 9**). Sometimes, the laser spot is wide enough to excite the Raman response of both the particle and the surrounding graphite, as revealed by the appearance of the D (1333 cm^{-1}), G (1579 cm^{-1}), and 2D (2682 cm^{-1}) bands. Raman peaks corresponding to these particles appear centered at about 88, 144, 213, 422, 523, and 621 cm^{-1} and can be all attributed to Cu_2O [32–34], evidencing the existence of particles of this oxide or Cu particles whose surface has been oxidized as a result of prolonged exposure to ambient air. It should be mentioned that, due to symmetry reasons, Cu is Raman inactive. Hence, detection of metallic Cu particles is not possible by using this spectroscopic technique. According to group theory, Cu_2O has six zone- center optical phonon modes which are classified as: $\Gamma = F_{2g} + 2F_{1u} + F_{2u} + E_u + A_{2u}$. The F_{2g} mode (~515 cm^{-1}) is Raman-active and the two F_{1u} modes (~144 and ~630 cm^{-1}) are IR active for a perfect Cu_2O lattice [32–34]. However, Cu_2O is frequently nonstoichiometric and defects (including O and Cu vacancies) may induce a breakdown of the selection rules and activate Raman inactive modes [33,34]. In addition, multiphonon processes can also be observed in our Raman spectra. In fact, the 213 cm^{-1} peak is attributed to a $2E_u$ overtone while the mode at ~422 cm^{-1} is due to a multiphonon process [33,34].

Preprints (www.preprints.org) | NOT PEER-REVIEWED | Posted: 25 March 2022 doi:10.20944/preprints202203.0347.v1

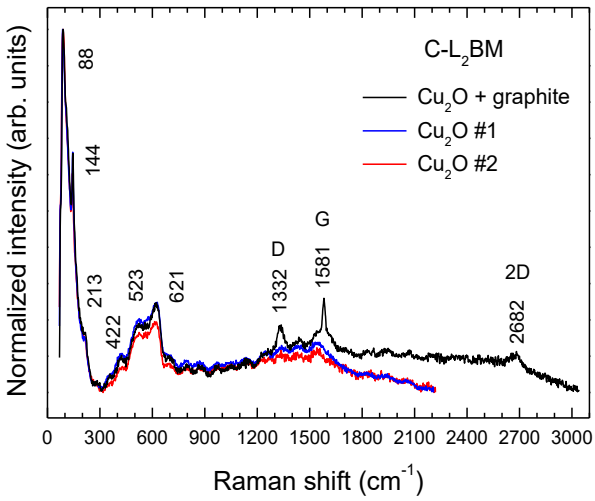

Figure 9. Raman spectra of small Cu_2O particles from the C-L2BM sample.

4. Conclusions

High-quality recycled graphites have been obtained from black masses, a common waste product generated in the recycling of spent batteries. Black masses from spent Zn/C alkaline and from lithium-ion batteries were assessed. Despite their different starting compositions, acid leaching was successfully used to separate the metal content present in the mentioned black masses. XRD patterns of the investigated samples reveal carbon-graphite as the principal crystalline phase. Only minor amounts of second phases were detected in some samples. Materials obtained from different types of black masses show uneven morphologies. SEM micrographs show densely packed agglomerates in the case of the graphite obtained from alkaline batteries, while rounded particles were observed for the materials obtained from LIBs black masses. EDX spectra and elemental mappings reveal that the obtained materials are mainly composed by carbon, with the exception of minor impurities, which indicate that acidic leaching was successful. Raman spectra of all the investigated samples mainly exhibit bands than can be attributed to crystalline graphite. In the case of the graphite obtained from the black mass of spent Zn/C alkaline batteries, the measured relative intensities (I_D/I_G) and ($I_{D'}/I_G$) bands, as well as the higher FWMH of the G band can be considered representative of crystalline graphite with a rather high density of defects. However, spectra from graphites obtained from black masses of spent LIBs can be considered representative of a good quality crystalline material with a rather low density of defects, as evidenced by the lower (I_D/I_G) and ($I_{D'}/I_G$) ratios and the lower FWMH of the G band. These results evidence the obtaining of a high-added value material from different kinds of spent batteries through acid leaching.

Author Contributions: Conceptualization, L.A., and F.A.L.; data curation, L.A., and C.D.-G..; resources, C.D.-G.; investigation, L.A., C.D.-G. and F.A.L.; methodology, L.A., and F.A.L.; writing—original draft, L.A., and C.D.-G.; writing—review and editing, L.A., C.D.-G. and F.A.L. All authors have read and agreed to the published version of the manuscript.

Funding: This work has been funded by the European Union's Horizon 2020 research and innovation program under grant agreement No 776851 (CarE Service) and by Banco Santander-UCM through project PR87/19-22613.

Institutional Review Board Statement: Not applicable.

Informed Consent Statement: Not applicable.

Data Availability Statement: Not applicable.

Acknowledgments: The authors thank Yarivith González and her Extractive Metallurgical group at the Consejo Nacional de Investigaciones Científicas y Técnicas (CONICET) for providing the black mass from smartphones lithium-ion batteries used in this study.

Conflicts of Interest: The authors declare no conflict of interest.

References

1. Moradi, B.; Botte, G.G. Recycling of graphite anodes for the next generation of lithium ion batteries. *J. Appl. Electrochem.* **2016**, *46*, 123–148, doi:10.1007/s10800-015-0914-0.
2. El-Hout, S.I.; Attia, S.Y.; Mohamed, S.G.; Abdelbasir, S.M. From waste to value-added products: Evaluation of activated carbon generated from leather waste for supercapacitor applications. *J. Environ. Manage.* **2022**, *304*, 114222, doi:10.1016/j.jenvman.2021.114222.
3. Chen, M.; Ma, X.; Chen, B.; Arsenault, R.; Karlson, P.; Simon, N.; Wang, Y. Recycling End-of-Life Electric Vehicle Lithium-Ion Batteries. *Joule* **2019**, *3*, 2622–2646, doi:10.1016/j.joule.2019.09.014.
4. Kang, D.H.P.; Chen, M.; Ogunseitan, O.A. Potential Environmental and Human Health Impacts of Rechargeable Lithium Batteries in Electronic Waste. *Environ. Sci. Technol.* **2013**, *47*, 5495–5503, doi:10.1021/es400614y.
5. Liu, J.; Shi, H.; Hu, X.; Geng, Y.; Yang, L.; Shao, P.; Luo, X. Critical strategies for recycling process of graphite from spent lithium-ion batteries: A review. *Sci. Total Environ.* **2021**, 151621, doi:10.1016/j.scitotenv.2021.151621.
6. Swain, B. Recovery and recycling of lithium: A review. *Sep. Purif. Technol.* **2017**, *172*, 388–403, doi:10.1016/j.seppur.2016.08.031.
7. Zheng, X.; Zhu, Z.; Lin, X.; Zhang, Y.; He, Y.; Cao, H.; Sun, Z. A Mini-Review on Metal Recycling from Spent Lithium Ion Batteries. *Engineering* **2018**, *4*, 361–370, doi:10.1016/j.eng.2018.05.018.
8. Ribeiro, J.S.; Freitas, M.B.J.G.; Freitas, J.C.C. Recycling of graphite and metals from spent Li-ion batteries aiming the production of graphene/CoO-based electrochemical sensors. *J. Environ. Chem. Eng.* **2021**, *9*, 104689, doi:10.1016/j.jece.2020.104689.
9. Yu, J.; He, Y.; Ge, Z.; Li, H.; Xie, W.; Wang, S. A promising physical method for recovery of $LiCoO_2$ and graphite from spent lithium-ion batteries: Grinding flotation. *Sep. Purif. Technol.* **2018**, *190*, 45–52, doi:10.1016/j.seppur.2017.08.049.
10. Yang, Y.; Song, S.; Lei, S.; Sun, W.; Hou, H.; Jiang, F.; Ji, X.; Zhao, W.; Hu, Y. A process for combination of recycling lithium and regenerating graphite from spent lithium-ion battery. *Waste Manag.* **2019**, *85*, 529–537, doi:10.1016/j.wasman.2019.01.008.
11. Badawy, S.M. Synthesis of high-quality graphene oxide from spent mobile phone batteries. *Environ. Prog. Sustain. Energy* **2016**, *35*, 1485–1491, doi:10.1002/ep.12362.
12. Alcaraz Romo, L.; López-Fernández, A.; García-Díaz, I.; Fernández, P.; Urbieta, A.; López, F.A. From spent alkaline batteries to $Zn_xMn_{3-x}O_4$ by a hydrometallurgical route: synthesis and characterization. *RSC Adv.* **2018**, *8*, 33496–33505, doi:10.1039/C8RA06789A.
13. Urbańska, W. Recovery of Co, Li, and Ni from Spent Li-Ion Batteries by the Inorganic and/or Organic Reducer Assisted Leaching Method. *Minerals* **2020**, *10*, 555, doi:10.3390/min10060555.
14. Li, L.; Ge, J.; Wu, F.; Chen, R.; Chen, S.; Wu, B. Recovery of cobalt and lithium from spent lithium ion batteries using organic citric acid as leachant. *J. Hazard. Mater.* **2010**, *176*, 288–293, doi:10.1016/j.jhazmat.2009.11.026.
15. Gerold, E.; Schinnerl, C.; Antrekowitsch, H. Critical Evaluation of the Potential of Organic Acids for the Environmentally Friendly Recycling of Spent Lithium-Ion Batteries. *Recycling* **2022**, *7*, 4, doi:10.3390/recycling7010004.
16. Qiu, T.; Yang, J.G.; Bai, X.J.; Wang, Y.L. The preparation of synthetic graphite materials with hierarchical pores from lignite by one-step impregnation and their characterization as dye absorbents. *RSC Adv.* **2019**, *9*, 12737–12746, doi:10.1039/c9ra00343f.
17. Franklin, R.E. The structure of graphitic carbons. *Acta Crystallogr.* **1951**, *4*, 253–261, doi:10.1107/S0365110X51000842.
18. Li, Q.; Chen, J.; Fan, L.; Kong, X.; Lu, Y. Progress in electrolytes for rechargeable Li-based batteries and beyond. *Green Energy Environ.* **2016**, *1*, 18–42, doi:10.1016/j.gee.2016.04.006.
19. Lavi, O.; Luski, S.; Shpigel, N.; Menachem, C.; Pomerantz, Z.; Elias, Y.; Aurbach, D. Electrolyte Solutions for Rechargeable Li-Ion Batteries Based on Fluorinated Solvents. *ACS Appl. Energy Mater.* **2020**, *3*, 7485–7499, doi:10.1021/acsaem.0c00898.
20. Bokobza, L.; Bruneel, J.-L.; Couzi, M. Raman Spectra of Carbon-Based Materials (from Graphite to Carbon Black) and of Some Silicone Composites. *C* **2015**, *1*, 77–94, doi:10.3390/c1010077.

21. Bai, Y.; Zhao, X.; Li, T.; Lv, Z.; Lv, S.; Han, H.; Yin, Y.; Wang, H. First-principles investigation in the Raman and infrared spectra of sp^3 carbon allotropes. *Carbon N. Y.* **2014**, *78*, 70–78, doi:10.1016/j.carbon.2014.06.050.
22. Ferrari, A.C.; Basko, D.M. Raman spectroscopy as a versatile tool for studying the properties of graphene. *Nat. Nanotechnol.* **2013**, *8*, 235–246, doi:10.1038/nnano.2013.46.
23. Pimenta, M.A.; Dresselhaus, G.; Dresselhaus, M.S.; Cançado, L.G.; Jorio, A.; Saito, R. Studying disorder in graphite-based systems by Raman spectroscopy. *Phys. Chem. Chem. Phys.* **2007**, *9*, 1276–1290, doi:10.1039/B613962K.
24. Ferrari, A.C. Raman spectroscopy of graphene and graphite: Disorder, electron–phonon coupling, doping and nonadiabatic effects. *Solid State Commun.* **2007**, *143*, 47–57, doi:10.1016/j.ssc.2007.03.052.
25. Jorio, A. Raman Spectroscopy in Graphene-Based Systems: Prototypes for Nanoscience and Nanometrology. *ISRN Nanotechnol.* **2012**, *2012*, 1–16, doi:10.5402/2012/234216.
26. May, P.; Lazzeri, M.; Venezuela, P.; Herziger, F.; Callsen, G.; Reparaz, J.S.; Hoffmann, A.; Mauri, F.; Maultzsch, J. Signature of the two-dimensional phonon dispersion in graphene probed by double-resonant Raman scattering. *Phys. Rev. B* **2013**, *87*, 075402, doi:10.1103/PhysRevB.87.075402.
27. López-Díaz, D.; López Holgado, M.; García-Fierro, J.L.; Velázquez, M.M. Evolution of the Raman Spectrum with the Chemical Composition of Graphene Oxide. *J. Phys. Chem. C* **2017**, *121*, 20489–20497, doi:10.1021/acs.jpcc.7b06236.
28. Kaniyoor, A.; Ramaprabhu, S. A Raman spectroscopic investigation of graphite oxide derived graphene. *AIP Adv.* **2012**, *2*, 032183, doi:10.1063/1.4756995.
29. Ferrari, A.C.; Robertson, J. Origin of the 1150 − cm-1 Raman mode in nanocrystalline diamond. *Phys. Rev. B* **2001**, *63*, 121405, doi:10.1103/PhysRevB.63.121405.
30. Cançado, L.G.; Jorio, A.; Pimenta, M.A. Measuring the absolute Raman cross section of nanographites as a function of laser energy and crystallite size. *Phys. Rev. B* **2007**, *76*, 064304, doi:10.1103/PhysRevB.76.064304.
31. Yoshida, A.; Kaburagi, Y.; Hishiyama, Y. Full width at half maximum intensity of the G band in the first order Raman spectrum of carbon material as a parameter for graphitization. *Carbon N. Y.* **2006**, *44*, 2333–2335, doi:10.1016/j.carbon.2006.05.020.
32. Singhal, A.; Pai, M.R.; Rao, R.; Pillai, K.T.; Lieberwirth, I.; Tyagi, A.K. Copper(I) Oxide Nanocrystals – One Step Synthesis, Characterization, Formation Mechanism, and Photocatalytic Properties. *Eur. J. Inorg. Chem.* **2013**, *2013*, 2640–2651, doi:10.1002/ejic.201201382.
33. Zhang, X.; Mauger, A.; Lu, Q.; Groult, H.; Perrigaud, L.; Gendron, F.; Julien, C.M. Synthesis and characterization of LiNi1/3Mn1/3Co1/3O2 by wet-chemical method. *Electrochim. Acta* **2010**, *55*, 6440–6449, doi:10.1016/j.electacta.2010.06.040.
34. Dawson, P.; Hargreave, M.M.; Wilkinson, G.R. The dielectric and lattice vibrational spectrum of cuprous oxide. *J. Phys. Chem. Solids* **1973**, *34*, 2201–2208, doi:10.1016/S0022-3697(73)80067-8.